



**HAL**  
open science

## Hybrid Multimodal Contrast Agent for Multiscale In Vivo Investigation of Neuroinflammation

Szilvia Karpati, Violaine Hubert, Ines Hristova, Frederic Lerouge, Frédéric Chaput, Chantal Andraud, Yann Bretonnière, Akos Banyasz, Guillaume Micouin, Maelle Monteil, et al.

### ► To cite this version:

Szilvia Karpati, Violaine Hubert, Ines Hristova, Frederic Lerouge, Frédéric Chaput, et al.. Hybrid Multimodal Contrast Agent for Multiscale In Vivo Investigation of Neuroinflammation. *Nanoscale*, 2021, <10.1039/D0NR07026B>. <hal-03134034>

**HAL Id: hal-03134034**

**<https://hal.science/hal-03134034v1>**

Submitted on 8 Feb 2021

**HAL** is a multi-disciplinary open access archive for the deposit and dissemination of scientific research documents, whether they are published or not. The documents may come from teaching and research institutions in France or abroad, or from public or private research centers.

L'archive ouverte pluridisciplinaire **HAL**, est destinée au dépôt et à la diffusion de documents scientifiques de niveau recherche, publiés ou non, émanant des établissements d'enseignement et de recherche français ou étrangers, des laboratoires publics ou privés.



HAL Authorization

# Hybrid Multimodal Contrast Agent for Multiscale *In Vivo* Investigation of Neuroinflammation

Szilvia Karpati<sup>a</sup>, Violaine Hubert<sup>b</sup>, Inès Hristovska<sup>c</sup>, Frédéric Lerouge<sup>a\*</sup>, Frédéric Chaput<sup>a</sup>, Yann Bretonnière<sup>a</sup>, Chantal Andraud<sup>a</sup>, Akos Banyasz<sup>a</sup>, Guillaume Micouin<sup>a</sup>, Maëlle Monteil<sup>d</sup>, Marc Lecouvey<sup>d</sup>, Marion Mercey-Ressejac<sup>e</sup>, Arindam Dey<sup>e</sup>, Patrice N. Marche<sup>e</sup>, Mikael Lindgren<sup>f</sup>, Olivier Pascual<sup>c</sup>, Marlène Wiart<sup>b</sup>, Stephane Parola<sup>a\*</sup>

*a* Université de Lyon, Ecole Normale Supérieure de Lyon, CNRS UMR 5182, Université Lyon 1, Laboratoire de Chimie, 46 allée d'Italie, F69364 Lyon, France

*b* Univ-Lyon, CarMeN laboratory, Inserm U1060, INRA U1397, INSA Lyon, Université Claude Bernard Lyon 1, F-69600, Oullins, France

*c* Institut NeuroMyoGène, Université Claude Bernard Lyon 1, CNRS UMR 5310, INSERM U1217, Université Lyon, Villeurbanne 69100, France

*d* Université Sorbonne Paris Nord, Laboratoire CSPBAT, CNRS UMR 7244, F-93017 Bobigny Cedex, France

*e* Institute for Advanced Biosciences, Université Grenoble-Alpes, INSERM U1209, CNRS UMR5309, La Tronche, France.

*f* Norwegian University of Science and Technology - Department of Physics, Høgskoleringen 5, Realfagbygget, 7491 Trondheim, Norway

\* corresponding author

## Abstract

Neuroinflammation is a process common to several brain pathologies. Despite its medical relevance, it still remains poorly understood; there is therefore a need to develop new *in vivo* imaging strategies to monitor inflammatory processes longitudinally. We here present the development of a hybrid imaging nanoprobe named **NP3**, that was specifically designed to get internalized by phagocytic cells and imaged *in vivo* with MRI and bi-photon microscopy. **NP3** is composed of a 16 nm core of gadolinium fluoride (GdF<sub>3</sub>), coated with bisphosphonate polyethylene glycol (PEG) and functionalized with a Lemke-type fluorophore (LEM-A). It has a hydrodynamic diameter of 28±8 nm and a zeta potential of -42±6 mV. The MR relaxivity ratio at 7T is  $r_1/r_2 = 20$ ; therefore, **NP3** is well suited as a T<sub>2</sub>/T<sub>2</sub>\* contrast agent. *In vitro* cytotoxicity assessments performed on four human cell lines revealed no toxic effects of **NP3**. In addition, **NP3** is internalized by macrophages *in vitro* without inducing inflammation or cytotoxicity. *In vivo*, uptake of **NP3** has been observed in the spleen and the liver. **NP3** has a prolonged vascular remanence, which is an advantage for macrophage uptake *in vivo*. The proof-of-concept that **NP3** may be used as a contrast agent targeting phagocytic cells is provided in an animal model of ischemic stroke in transgenic CX3CR1-GFP/+ mice using three complementary imaging modalities: MRI, intravital two-photon microscopy and phase contrast imaging with synchrotron X-rays. In summary,

32 **NP3** is a promising preclinical tool for the multiscale and multimodal investigation of  
33 neuroinflammation.

## 34 **Introduction**

35 Stroke is one of the leading causes of mortality worldwide accounting for 11.8% of global deaths.<sup>1</sup>  
36 Ischemic stroke is induced by transient or permanent occlusion of a cerebral artery.<sup>2</sup> The perturbation  
37 of blood flow leads to neuronal death in the most severely hypoperfused areas. In addition, a complex  
38 sequence of inflammatory events occurs following ischemic stroke, among which the activation of  
39 infiltrating and brain resident macrophages (microglia).<sup>3</sup> This neuroinflammatory response may lead to  
40 secondary brain damage and thus represents a potential therapeutic target. However, the complex role  
41 of neuroinflammation is not well understood to date. There is thus a need to develop new *in vivo*  
42 preclinical imaging strategies to follow inflammatory processes longitudinally at the acute stage of  
43 ischemic stroke, in order to better understand the pathophysiology, as well as to monitor the effects of  
44 anti-inflammatory treatments prior to their clinical translation.

45 Today, PET imaging of microglia activation using 18 kDa translocator protein (TSPO) tracers is at the  
46 forefront for translational in-vivo molecular imaging of neuroinflammation following stroke.<sup>4</sup> One  
47 limitation of this approach, however, is that at the acute stage of ischemic stroke (<72h), the number  
48 of activated microglia is below the limit of detection. Therefore currently PET imaging cannot be used  
49 to monitor neuroinflammation in this crucial time-window, where immunomodulatory treatments may  
50 be the most effective. The noninvasive nature of MRI and CT, in conjunction with their wide availability,  
51 make them particularly suitable for longitudinal neurologic imaging studies. Magnetic resonance  
52 imaging (MRI) or computed tomography (CT) coupled with the administration of metallic nanoparticles  
53 (such as iron oxides) represents an attractive tool for studying inflammation.<sup>5,6</sup> After their intravenous  
54 injection, the nanoparticles get internalized by activated phagocytic cells, mostly macrophages. Since  
55 phagocytic cells strongly participate in the development of inflammation processes, these imaging  
56 approaches are used as a surrogate marker of inflammatory processes. The advantage of using metal-  
57 based nanoparticles for this purpose is the possibility to combine complementary imaging modalities  
58 at different scales to track the labelled macrophages. One of the limitations of these techniques,  
59 however, is the fact that the signals seen on postcontrast images may have different origins than  
60 nanoparticle-labelled cells, for instance microhemorrhages or microcalcifications. One way to address

61 this issue is to design contrast agents that may be imaged with element-specific imaging tools, for  
62 instance fluorine for MRI<sup>7</sup> and gadolinium for spectral photon counting CT.<sup>8</sup> In addition, to further  
63 validate the biological substrate of MR and CT signals, there is a need to complement these techniques  
64 with imaging tools that are better resolved spatially and provide information about specific immune  
65 cells. Intravital two-photon induced fluorescence imaging is a good candidate due to its high sensitivity,  
66 resolution at sub-cellular scale, the possibility of real-time monitoring and the availability of transgenic  
67 mice such as CX3CR1-GFP/+ mice that have green fluorescent microglia and macrophages.<sup>9</sup>

68 Consequently, the aim of our study was to design a multimodal contrast agent adapted simultaneously  
69 for three imaging modalities (MRI, CT and two-photon microscopy) and optimized for the passive  
70 targeting of phagocytic cells. In addition, because our primary application is ischemic stroke, we added  
71 the specification that our imaging probe should be able to cross the blood brain barrier (BBB) following  
72 focal cerebral ischemia. Nanoparticles are well-suited for this aim because they circulate longer than  
73 small molecular weight contrast agent and hence can accumulate in inflammatory regions with high  
74 phagocytic activity. Because gadolinium is particularly well-suited for both MRI and spectral photon  
75 counting CT [2], we here propose to use functionalized gadolinium fluoride (GdF<sub>3</sub>) nanoparticles as a  
76 contrast platform.

77 Due to its very low solubility (less than  $3 \cdot 10^{-5}$  mol L<sup>-1</sup>) in aqueous media,<sup>10</sup> GdF<sub>3</sub> is considered as one of  
78 the most stable gadolinium compounds. Moreover, nanostructured materials concentrate a high  
79 amount of gadolinium ions, giving rise to high contrast-to-noise ratio both in MRI and CT. Recently, we  
80 demonstrated that GdF<sub>3</sub> nanoparticles were optimal for *in vivo* angiography with spectral photon  
81 counting CT, due to their efficient X-ray attenuation properties and long vascular remanence.<sup>11</sup>

82 In the present work, size and coating of the GdF<sub>3</sub> platform were finely tuned to allow the passive  
83 targeting of phagocytic cells. The probe was further functionalized with a dedicated two-photon  
84 microscopy fluorophore. This paper reports the synthesis and characterization of this novel imaging  
85 nanoprobe. We verified that the nanoprobe was internalized *in vitro* by bone-marrow derived  
86 macrophages. We provide data on cytotoxicity as well as *in vivo* biodistribution and pharmacokinetic.  
87 Finally, the proof-of-concept of its potential for multiscale and multimodal imaging of  
88 neuroinflammation was obtained in a murine model of ischemic stroke using three complementary

89 imaging modalities: MRI, intravital two-photon microscopy and phase contrast imaging with  
90 synchrotron X-rays.

## 91 **Experimental**

### 92 **Synthesis of NP1**

93 4.83 g (0.013 mol) of GdCl<sub>3</sub>·6H<sub>2</sub>O (Alfa Aesar 99.9%) was stirred at room temperature in 2 mL of  
94 ethylene glycol (EG) until complete dissolution and was further diluted with 3 mL of 2-pyrrolidinone.  
95 This solution was added to a solution of 1.1 mL (0.0316 mol) 50% hydrofluoric acid in 24 mL of 2-  
96 pyrrolidinone. The mixture was then heated up to 170°C for 1.5 h in a 50 mL stainless steel Teflon lined  
97 digestion pressure vessel. The obtained suspension was cooled down to room temperature and the  
98 particles were precipitated in acetone. The colloidal nanoparticles were purified by several  
99 centrifugation-redispersion cycles using methanol as washing solvent. After purification, the  
100 nanoparticles were suspended in water and freeze-dried for further use.

### 101 **Synthesis of NP2 and NP3**

102 First step: 600 mg of GdF<sub>3</sub> NP were suspended in 2 mL of ultrapure water. To this suspension was added  
103 a solution of a mixture of two types of bifunctional bisphosphonate-terminated PEGs in water: 40.3 mg  
104 (4.67 10<sup>-5</sup> mol; 5mol% of total ligand quantity) of **2** and 899 mg (8.87 10<sup>-4</sup> mol) of **1** in 2 mL of ultrapure  
105 water. The homogeneous suspension was magnetically stirred at 80°C for 2h and stirred at room  
106 temperature for one night. The as prepared functionalized nanoparticles **NP2** were subjected to dialysis  
107 for one week to remove excess ligand and then were freeze-dried. In a second step a suspension of **NP2**  
108 (452 mg in 1.5 mL of water) was added to a solution of **3** (5.5 mg) in ethylene glycol (6.5 mL). The  
109 mixture was heated to 150°C and stirred for 5h. The obtained fluorescent and coated NPs (**NP3**) were  
110 first precipitated in acetone, washed with ethanol, and centrifuged several times, until the supernatant  
111 becomes colorless.

### 112 **Analysis of particle morphology and composition**

113 DLS and Zeta potential measurements were performed on aqueous suspensions of the particles, by a  
114 Malvern Instruments Nano ZS. XPS analysis was carried out by PHI Quantera SXM instrument, with  
115 monochromatic Al K $\alpha$  source. TEM images were acquired using a JEOL JEM 1400 equipped with a Gatan  
116 Orius 600 camera and operated at 120kV. XPS measurements were carried out with a PHI Quantera

117 SXM photoelectron spectrometer using Al K $\alpha$  radiation ( $h\nu$  1486.7 eV). MultiPak software was used for  
118 the fitting procedure.

### 119 **Two-photon absorption spectroscopic study**

120 For two-photon spectroscopic study the excitation source was a tunable femtosecond Ti-sapphire laser  
121 (Chameleon Ultra I, Coherent) producing 140 fs pulses. The excitation beam was focused by a 100 mm  
122 focal length lens into a 10x10 mm spectroscopic quartz (QZS) cell containing the sample. The emitted  
123 fluorescence was collected at right angle and delivered to a spectrometer (AvaSpec-EVO, Avantes) via  
124 an optical fiber. The cell position was adjusted so that the optical path was minimized in the cell on  
125 both the excitation and the detection side; this allowed reducing artefacts due to inner-filter effects  
126 and scattering. Additionally, low-pass filters were used between the cell and the entrance of the fiber  
127 to prevent the scattered laser light from entering the spectrometer as much as possible. Here  
128 fluorescein in a pH 13 aqueous solution was used as the two-photon reference standard.<sup>12</sup>

### 129 **Cytotoxicity assays**

130 Cell Lines: **NP3** nanoparticle potential cytotoxicity was assessed on four human cell lines, all supplied  
131 by the American Type Culture Collection (ATCC). A549, epithelial-like cells from human lung, were  
132 cultivated in DMEM 4.5 g L<sup>-1</sup> glucose + GlutaMAX medium supplemented with 10% fetal calf serum (FCS)  
133 and 1% penicillin-streptomycin. THP-1, monocytes from human peripheral blood, were cultivated in  
134 RPMI 1640 + GlutaMAX medium supplemented with 10% FCS, 1% penicillin-streptomycin, 1% pyruvate  
135 and 4.5 g L<sup>-1</sup> glucose. HepG2, human hepatocytes, were cultivated in MEM + GlutaMAX medium  
136 supplemented with 10% FCS, 1% penicillin-streptomycin and 1% pyruvate. Finally, HEK 293T, embryonic  
137 kidney cells from human, were cultivated in the same medium than HepG2 cells. Cell Survival Assays:  
138 **NP3** impact on cell lines was evaluated using two complementary assays: the LDH (Lactate  
139 Dehydrogenase) assay, assessing cell membrane damages and the MTT (3-(4,5-[dimethylthiazol](#)-2-yl)-  
140 2,5-di[phenyl](#)tetrazolium bromide) assay, assessing mitochondrial activity. Briefly, the different cell lines  
141 were seeded in 96-well plates at 10<sup>5</sup> cells/mL for A549, HEK and HepG2, and 5.10<sup>5</sup> cells/mL for THP-1,  
142 and incubated for 24h at 37°C and 5% CO<sub>2</sub>. After 24h, cells were exposed to different **NP3**  
143 concentrations (0.5 nM to 5000 nM). Cell survival assays have been performed at 48 hours and 72 hours  
144 after **NP3** incubation. For LDH assay, cells were incubated with 100  $\mu$ L of CytoToxOne reagent for  
145 10 minutes at 22°C. 50  $\mu$ L of Stop solution were then added in each well and cell death is measured by

146 fluorescence with ELISA plate reader (Victor, Perkin Elmer) at  $\lambda_{ex} = 544$  nm and  $\lambda_{em} = 572$  nm. For MTT  
147 assay, 10  $\mu$ L of MTT Sigma-Aldrich solution (5 mg mL<sup>-1</sup> in PBS) were added to each well, and the 96-well  
148 plates were incubated for 2 hours at 37°C. 100  $\mu$ L of lysis buffer (SDS 10%) were then added to each  
149 well, and after 3 hours of agitation, cell viability was determined by absorption measurement  
150 ( $\lambda = 570$  nm) with ELISA plate reader (Victor, Perkin Elmer).

### 151 **Animal model and *in vivo* experimental timeline**

152 All procedures involving animals and their care were carried out according to the European regulation  
153 for animal use (EEC Council Directive 2010/63/UE, OJ L 276, Oct. 20, 2010). This study was approved by  
154 our local ethic committee “Comité d’éthique pour l’Expérimentation Animale Neurosciences Lyon”  
155 (CELYNE - CNREEA number: C2EA – 42).

156 At D0, transgenic CX3CR1-GFP/+ mice expressing green fluorescent protein (eGFP) in  
157 microglia/macrophages were subjected to a model of ischemic stroke (males, n=4). Permanent  
158 occlusion of the distal middle cerebral artery (pMCAo) was induced in the anesthetized (isoflurane, 2%,  
159 ISO-VET, Piramal Healthcare, Morpeth, UK) animals, using the application of iron chloride (10% FeCl<sub>3</sub>)  
160 solution, according to the procedure described previously by Karatas et al.<sup>13</sup> One mouse not submitted  
161 to pMCAo served as control. One day after the occlusion (D1), all the mice (n=5) underwent a basal MRI  
162 session to assess the presence of an ischemic lesion. Immediately after, the mice were injected into the  
163 tail vein with 2 mmol kg<sup>-1</sup> of **NP3** (n=5). Following the injection, a subgroup of mice (pMCAo mouse,  
164 n=2; control mouse; n=1) was submitted to a second surgical intervention for intravital two-photon  
165 microscopy imaging: after the skull was thoroughly thinned, a 6 mm diameter polyamide (MRI-  
166 compatible) implant was placed over an area encompassing both the ischemic lesion and some  
167 extralesional tissue. On the same day (D1), these mice underwent a 2 hours-two-photon excitation  
168 microscopy (TPEM) imaging session. In order to have pre-**NP3** and post-**NP3** TPEM images, the control  
169 mouse was intravenously injected with **NP3** during the TPEM session and was also imaged 24 hours  
170 after **NP3** injection (D2). To assess the potential of TPEM for **NP3** longitudinal follow-up, one of the pMCAo  
171 mice was submitted to a second TPEM imaging session. Finally, all mice (n=5) underwent a post-**NP3**  
172 MRI session 48 hours following **NP3** injection (D3) and were then euthanized. *Ex vivo* X-ray phase  
173 contrast imaging was performed on the brain of pMCAo mouse.

### 174 ***In vitro* and *in vivo* MRI**

175 All the MRI exams were performed on a 7T horizontal-bore Bruker Advance II rodent imaging system  
176 (Bruker Biospin, Ettlingen, Germany). For the *in vivo* MR imaging exams, mouse anaesthesia was  
177 induced with a mixture of air and 3.5% isoflurane and maintained with 2% isoflurane. The animals were  
178 placed in an MRI-compatible mouse cradle, and the body temperature was monitored thanks to  
179 circulating heated water. Relaxivity measurements: To quantify the  $r_1$  and  $r_2$  relaxivities of **NP3** (in  $\text{mM}^{-1}$   
180  $\text{s}^{-1}$ ), phantoms have been prepared with a range of twelve gadolinium concentrations going from 0 to  
181 5 mM in saline. To reach the appropriate concentrations, **NP3** phantoms were prepared using a 0.5 M  
182 stock solution dissolved in saline. Measurements were then performed at 25°C.  $T_1$  maps were obtained  
183 from a fast imaging with steady-state procession (FISP) sequence (TE/TR=2.1/4.2 ms; Inversion time  
184 (TI): 73.8 ms; 32 echoes) by fitting an inversion/recuperation function to the data.  $T_2$  maps were  
185 obtained from a multiple spin-echo sequence (MSME; TE [interecho delay]/TR=50/5000 ms; 24 echoes)  
186 by fitting a monoexponential function to the data. Biodistribution and pharmacokinetic: To evaluate  
187 **NP3** biodistribution and pharmacokinetic, C57Bl/6 mice (males, n=4) were imaged using a 35 mm inner  
188 diameter whole-body transmit-receive coil for signal acquisition. To avoid movement artifacts due to  
189 the breathing, the acquired sequence was triggered on mouse respiratory rhythms. Abdominal axial  $T_1$   
190 images were obtained with a dynamic RARE 2D sequence (TE/TR = 7.51/960.77 ms; FA = 90; number of  
191 averages = 2; acquisition time 1.32 min; number of repetitions = 25). 37 slices were acquired from the  
192 top of the heart to the bottom of the liver, using a FOV of  $35 \times 35 \text{ mm}^2$ , a slice thickness of 1 mm and a  
193 matrix of  $128 \times 128$ . **NP3** ( $2.0 \text{ mmol kg}^{-1}$ ) was injected as a bolus *in vivo* in the magnet between the  
194 second and the third repetitions. MR signal changes in time were analyzed in regions of interest (ROI)  
195 and normalized using pre-contrast values. Imaging of stroke-induced animals: A 50 mm inner diameter  
196 birdcage coil was used for transmission and a 15 mm diameter surface coil was used for reception. The  
197 following axial sequences were used: a spin-echo  $T_2$ -weighted image ( $T_2$ -WI), TE/TR = 43.8/5000 ms,  
198 bandwidth = 40 kHz, number of averages = 6, acquisition time 12 min; a  $T_2$ -star gradient-echo (GRE)  
199 FLASH sequence ( $T_2^*$ -WI), TE/TR= 6/750 ms, bandwidth= 40 kHz, flip angle (FA)= 20°, number of  
200 averages = 8, acquisition time 19 min. For each sequence, 25 slices were acquired from the olfactory  
201 bulb to the cerebellum of the mice, using a field of view (FOV) of  $20 \times 20 \text{ mm}^2$ , a slice thickness of 500  $\mu\text{m}$   
202 and a matrix size of  $256 \times 256$ .

## 203 **Two-photon excitation microscopy (TPEM)**

204 For the *in vivo* TPEM imaging sessions, mice have been anesthetized with a mixture of ketamine  
205 (100 mg kg<sup>-1</sup>) and medetomidine (1 mg kg<sup>-1</sup>). Their body temperature was maintained at 37 °C using a  
206 heating pad. TPEM observations were performed on a Bruker Ultima microscope (Insight 3X laser,  
207 Spectra Physics), equipped with a 20x water-immersion objective (0.95 N.A. Olympus). Green (CX3CR1-  
208 GFP/+ cells) and red (**NP3** particles) fluorescence were separated by a 560 nm dichroic mirror coupled  
209 to 525/50 nm and 650/40 emission filters.

210 30-45 consecutive Z-stacks were acquired at a depth of 50-150 μm, with a step size of 1 μm and a  
211 resolution of 521x521 pixels. ImageJ and Icy (open source software created by BioImage Analysis Lab,  
212 Institut Pasteur, France; <http://icy.bioimageanalysis.org/>) were used for image treatment, and drift  
213 correction was applied with a custom-written Matlab software (used for image correction for drift  
214 during the acquisition).

### 215 **X-ray phase contrast tomography**

216 For *ex vivo* phase contrast tomography, mice have been euthanized by intracardiac perfusion with 4%  
217 PFA. Brains were then extracted and dehydrated in successive ethanol baths. In-line phase contrast  
218 tomography was performed on beamline ID17 of the European Synchrotron Radiation Facility (ESRF) in  
219 Grenoble at 26 keV. An indirect detection-based detector with a LuAg scintillator, standard microscope  
220 optics and a 2048x2048 pixel CCD camera was positioned 3 m from the sample to obtain phase contrast.  
221 The whole-brain data set was acquired at an isotropic pixel size of 7.5 μm. Acquisition time of the 3000  
222 projections was <5 minutes per brain. Reconstruction was performed with Paganin algorithm by setting  
223  $\gamma/\beta$  to 1000 as in.<sup>14</sup>

## 224 **Results and Discussion**

### 225 **Nanoparticle core synthesis (NP1)**

226 The synthesis of the GdF<sub>3</sub> inorganic core (**NP1**) was adapted from a previously described method<sup>11</sup>  
227 under solvothermal conditions in a mixture of ethylene glycol (EG) and 2-pyrrolidinone.<sup>15-17</sup> The  
228 originality of this method consists in the generation of various complexes involving F<sup>-</sup> and Gd<sup>3+</sup> ions  
229 (Scheme 1A) leading to an improved control of nanoparticle morphology and size distribution. As shown  
230 by transmission electron microscopy (TEM) observations (Fig. S1-A), **NP1** are spheroidal and slightly  
231 elongated. Their hydrodynamic diameter determined by dynamic light scattering (DLS) measurements

232 (Fig. S1-B) is  $16\pm 5$  nm, with low polydispersity (polydispersity index, PDI: 0.16). The X-ray powder  
233 diffraction (XRPD) pattern (Fig. S1-C) shows high crystallinity of **NP1** and comparison of the peaks to the  
234 reference pattern ICSD Card 00-012-0788 demonstrates the pure orthorhombic phase (*Pnma* space  
235 group) of  $GdF_3$ . The positive zeta potential  $+45\pm 10$  mV measured for **NP1** in water, suggests an excess  
236 of  $Gd^{3+}$  ions on the surface, which is in accordance with the observed 67.7 atomic % of gadolinium,  
237 determined by X-ray photoelectron spectroscopy (XPS) analysis (Table S1). Furthermore, this elemental  
238 composition analysis reveals a F/Gd atomic ratio of 0.39 at the surface. Such small ratio (expected F/Gd  
239 ratio is 3) is explained by two aspects. First, the surface composition of a nanoparticle is always different  
240 from the bulk composition (surface effects, crystal defects etc.) and segregation of elements is  
241 frequently observed.<sup>18</sup> XPS is a surface scanning technique, with a penetration depth of a few  
242 nanometers. In our case it was approximately 3 nm, therefore the observed composition was not the  
243 composition of bulk  $GdF_3$ . The second reason is that in our synthesis conditions F/Gd is kept lower than  
244 the stoichiometric ratio, because  $F^-$  excess induces in the case of gadolinium a mixture of two crystalline  
245 phases: orthorhombic and hexagonal. However, as it was mentioned before, according to X-ray powder  
246 crystallographic measurements, the overall crystalline phase corresponds effectively to the  
247 orthorhombic  $GdF_3$  phase (Fig S1-C). According to attenuated total reflection Fourier-transform  
248 infrared spectroscopy (ATR-FTIR) measurements, small organic capping molecules identified as the  
249 open form of solvent molecule 2-pyrrolidinone, are present on the surface (Fig. S2-A).

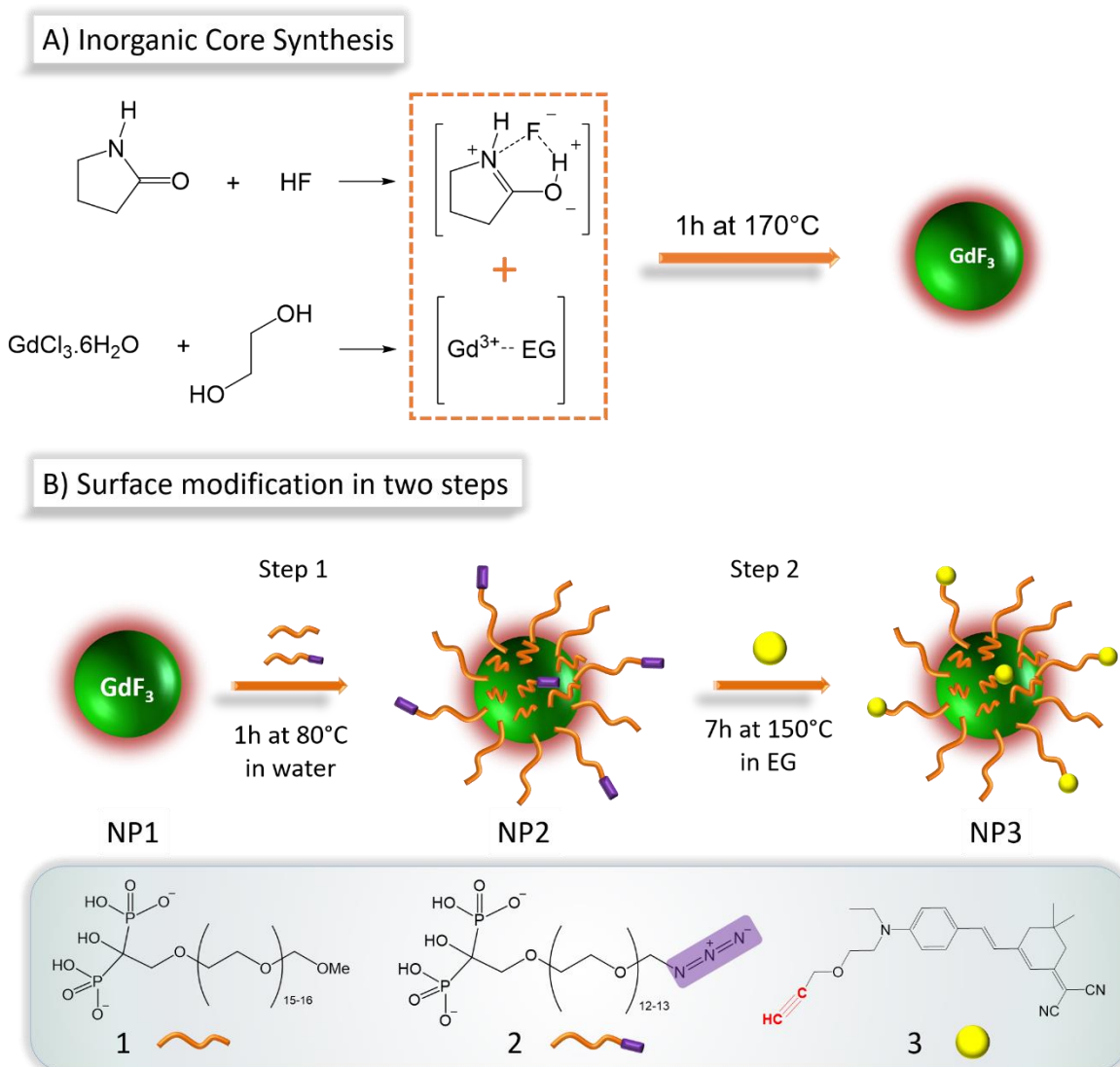
250

### 251 **Core-shell nanoparticles (NP2)**

252 The surface modifications of **NP1** was achieved following a two-step approach presented in Scheme 1-  
253 B. The first step consists in the preparation of functional particles **NP2**, through the grafting of a mixture  
254 of two bisphosphonate PEG derivatives with and without azide reactive groups (compounds **1** and **2**,  
255 respectively). The synthesis of these ligands developed by Lecouvey *et al.* has been described in detail  
256 elsewhere.<sup>19</sup> The bisphosphonate functions allow strong anchoring via multidentate chelation of  
257 gadolinium ions.<sup>20,21</sup> While ligand **1** is used to ensure biocompatibility, **2** allows coupling with the  
258 fluorophore **3** through its  $-N_3$  group. The molar percentages of ligand **1** and ligand **2** were set at  
259 respectively 95% and 5%. This ratio was optimized taking into consideration the stability of the particle  
260 in biological media and the optical properties for appropriate two-photon fluorescence imaging. The  
261 second step focuses on the coupling of fluorophore **3** (the synthesis of **3** is described in ref.<sup>22</sup>) with the

262 azide functions on the PEG-coated nanoparticle **NP2**.

263



264

265 **Scheme 1 A)** Solvothermal synthesis of  $\text{GdF}_3$  nanoparticles (**NP1**). The solvent, 2-Pyrrolidinone is complexing the fluoride  
266 ion (source of fluoride is HF) and ethylene glycol chelates Gadolinium (III) ions (from  $\text{GdCl}_3$ ). The mixture is heated to  $170^\circ\text{C}$   
267 for 1h in a Teflon lined autoclave to give **NP1** nanoparticles. **B)** The surface of **NP1** is modified in two steps: first, PEG-ligands,  
268 **1** and **2** are grafted and chromophore **3** is coupled in a second step.

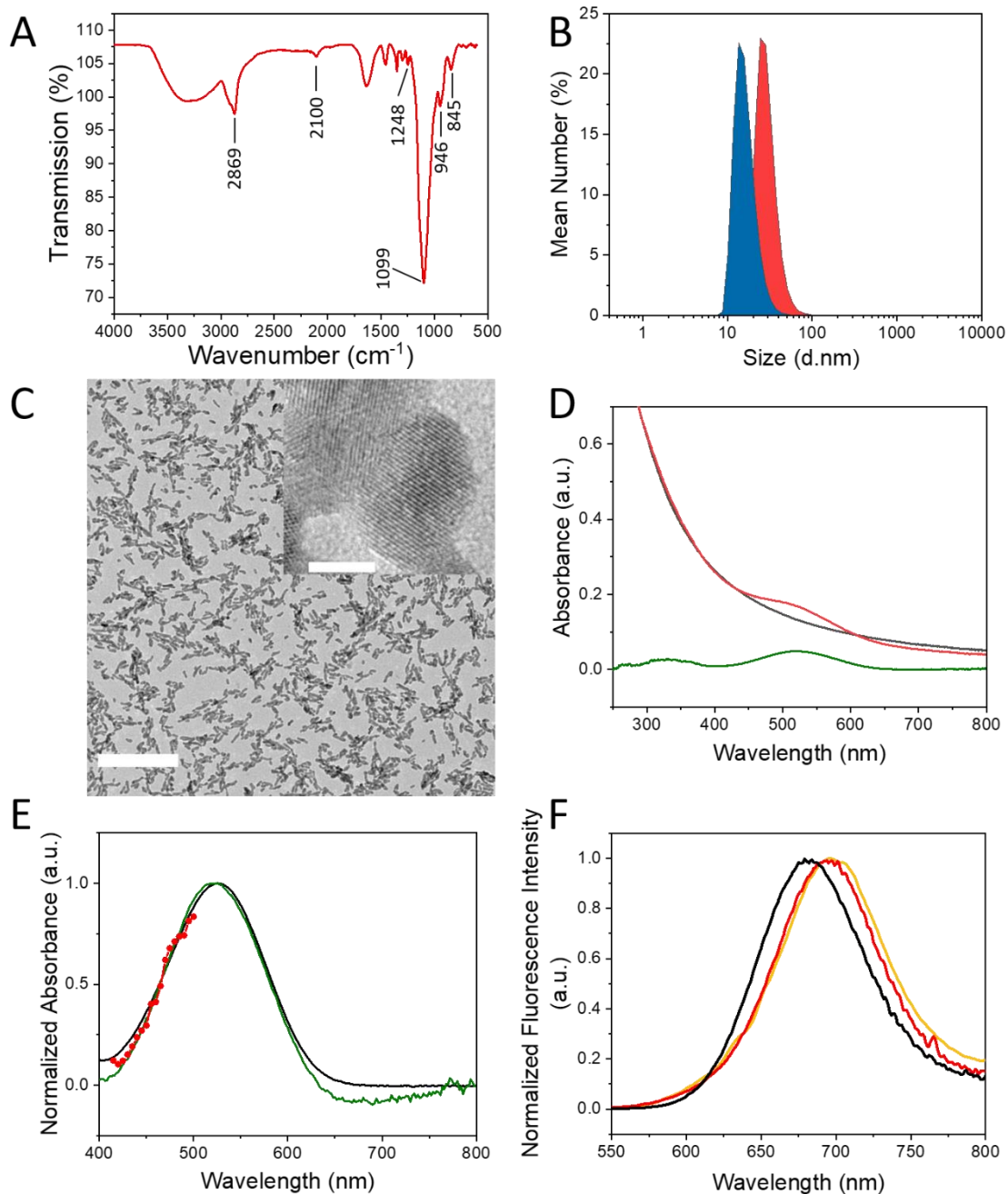
269

270 The success of multifunctional PEG grafting was first evaluated by ATR-FTIR spectroscopy. Infrared  
271 spectrum of **NP2** (Fig. 1-A) as compared to **NP1** (Fig. S2-A, red spectrum) shows typical signatures of  
272 PEG species, with bands at  $2869\text{ cm}^{-1}$  and around  $1100\text{ cm}^{-1}$  for ether C–H and C–O–C stretching modes  
273 respectively.<sup>23</sup> The presence of the organic layer around the particles was also evidenced by DLS (Fig. 1-  
274 B) where hydrodynamic diameter increases from  $16\pm 5\text{ nm}$  (blue signal) to  $21\pm 7\text{ nm}$  (red signal). Charge

275 surface of the particles was evaluated with zeta potential measurements, showing a switch from a  
276 positive (+45±10 mV) to a negative value (−28±3 mV) due to the deprotonated bisphosphonate  
277 moieties linked to surface gadolinium atoms. Grafting of PEG-ligands **1** and **2** on the particle was also  
278 evidenced by thermogravimetric analysis (TGA) (Fig. S2-B) where a significantly higher weight loss  
279 (29.3 %) corresponding to organics was observed in the case of **NP2** compared to **NP1**.

### 280 **Fluorophore coupling to NPs (NP3)**

281 One of the principal requirements for two-photon fluorescence imaging of biological media is that the  
282 dyes emit fluorescence in the red-near infrared (NIR) spectral range, where the autofluorescence from  
283 the medium is minimal and light is less scattered. The Lemke-type<sup>24</sup> fluorophore **3**, used in the present  
284 work was specifically designed for fluorescence imaging in biological media. As previously reported, this  
285 type of molecule was characterized by a strong dipolar donor-acceptor push-pull structure, which  
286 induces favorable optical spectroscopic properties suitable for imaging in the first biological  
287 transparency window (700-1000 nm).<sup>22,25,26</sup> Coupling of **3** with **NP2** was performed without use of  
288 copper catalyst, via thermally induced Huisgen-type 1,3-cycloaddition<sup>27</sup> to obtain **NP3**. Thermal  
289 activation of the reaction was preferred here to avoid use of toxic copper(II) ions for *in vivo* application.  
290 This coupling occurs between the azide functions on the surface of **NP2**, and the alkyne functions of  
291 fluorophore **3**, resulting in a strong bonding through imidazole cycle. In order to confirm the  
292 fluorophore grafting on **NP3**, infrared spectroscopy was used (Fig. S3-A). The vibration bands of PEG  
293 moieties (2869 cm<sup>-1</sup> and 1100 cm<sup>-1</sup>) and BP end-groups (1248 cm<sup>-1</sup> around 1099 cm<sup>-1</sup>, 946 cm<sup>-1</sup> and  
294 845 cm<sup>-1</sup> for P=O, P–O and P–O(H) stretching vibrations respectively)<sup>15,28</sup> remain unchanged while the  
295 one corresponding to –N<sub>3</sub> groups (2100 cm<sup>-1</sup>) disappears along with the reaction advancement (Fig. S3-  
296 A inset), clearly evidencing the coupling with **3**.



297

298 **Fig. 1 A)** FTIR-ATR spectra of **NP2** nanoparticles. **B)** DLS measurements of the particles before (**NP1**) any surface modification  
 299 (blue) and after PEGylation and fluorophore grafting (**NP2**) (red). **C)** TEM image of the particles after surface modification  
 300 (**NP3**). Scale bar is 50 nm for larger image and 5 nm for the inset. **D)** Absorption spectra of **NP3** (red line) and **NP2** (black  
 301 line) are compared. The difference of these two spectra (green line) reveals the absorbance of the chromophore without  
 302 the scattering due to the particles. **E)** Differential absorbance (green) showing the absorption bands of the chromophore  
 303 (520 and 326 nm) compared to the spectrum of compound **3** in ethylene glycol (black line). The normalized two-photon  
 304 absorption spectrum (red line+scatter) is reported on the same figure. for comparison. **F)** Normalized fluorescence emission  
 305 spectra upon one photon excitation of free dye (compound **3**, black line) in methanol and **NP3** nanoparticles (red line)  
 306 suspended in water. Upon excitation at 510 nm, the maximum emission values are 658 and 682 nm, respectively. The two-  
 307 photon fluorescence spectrum obtained upon 1000 nm excitation of aqueous dispersion of **NP3** is indicated in dark yellow.

308

309 Interestingly, in spite of water-insolubility of **3**, the purified nanoparticles **NP3** were perfectly  
310 dispersible in aqueous medium, resulting in a pale pink-color homogeneous colloidal suspension. DLS  
311 measurements of **NP3** showed a slight increase in the average hydrodynamic size ( $28\pm 8$  nm) due to the  
312 presence of the polymeric coating. The measured Zeta-potential value is  $-42\pm 6$  mV. The high stability  
313 of the particles is thus explained by both electrostatic and steric interactions. The authors attribute zeta  
314 potential decrease from  $-28\pm 3$  mV (**NP2**) to  $-42\pm 6$  mV (**NP3**) to the modification of coordination modes  
315 of bisphosphonate groups on the particle surface. The coordination of multidentate bisphosphonate  
316 moiety, which is the anchoring function of the ligands seem to be reorganized due to the heat-  
317 treatment during the coupling reaction. Increasing the proportion of not complexed P-O<sup>-</sup> bonds lead to  
318 the lower negative zeta potential. XPS analysis of the high-resolution spectrum centered on O 1s (Fig. S4  
319 C2) supports this hypothesis. The measured binding energy band was decomposed to two contributions  
320 with peak maxima at 532.21 eV (61.11%) and 530.70 eV (38.89%), which were attributed to O-Gd and  
321 (H)O-P binding energies respectively. XPS elemental analysis (Table S1) reveal F/Gd ratios of 0.39 and  
322 0.60 for **NP1** and **NP3** particles, respectively. The apparent Gd depletion is explained by partial shielding  
323 of surface gadolinium ions, due to the presence of the organic ligands (12.2 at% of carbon atoms on  
324 **NP3** compared to 0% on **NP1**) in the case of **NP3**. High-resolution XPS spectra (Fig. S4) show that the  
325 binding energy of Gd 3d<sub>5/2</sub> appears at 1187.8 eV for **NP1** and at 1188 eV for **NP3**. The peak Gd 4d<sub>5/2</sub>  
326 appears at 142.7 eV for **NP1** and at 143.4 eV for **NP3**, which are attributed to GdF<sub>3</sub> compound.<sup>29</sup> Upon  
327 functionalization the peaks of Gd 4d are not significantly changed, suggesting, that the inorganic core  
328 retains its composition. The peak F 1s was detected at 684. eV for **NP3**, which also corresponds to the  
329 form GdF<sub>3</sub>.<sup>29</sup>

330 **NP2** was incubated with compound **3** in the usual conditions, without heating, in order to confirm  
331 unambiguously that compound **3** is covalently bonded and not adsorbed through weak interactions  
332 with PEG chains present on the surface. The resulting mixture was purified through centrifugation  
333 cycles and analyzed by UV-visible absorption spectroscopy (Fig. S3-B). The resulting absorption  
334 spectrum showed only the scattering profile of the particles and no absorption band associated to the  
335 fluorophore was observed. This is consistent with the fact that **3** does not react without heating and  
336 conversely the covalent bonding of the fluorophore to the particle surface was confirmed for **NP3**.  
337 Finally, TEM observations were performed on **NP3** to verify the stability of the GdF<sub>3</sub> core during the  
338 heating process, (Fig. 1-C). TEM images showed similar morphology size and shape, as the initial

339 particles.

### 340 **Linear spectroscopy characterization of NP3**

341 Before using **NP3** for *in vivo* experiments, the preservation of the optical properties of **3** when coupled  
342 to the nanoparticle was evidenced by absorption and emission spectroscopy. The UV-visible spectrum  
343 of **3** was recorded in three different solvents to evaluate the effect of environment polarity on spectral  
344 properties (Fig. S5). In all three cases, a strong and structureless band appears between 400 and 650 nm  
345 accompanied by a smaller intensity band at shorter wavelengths (from 250 to 400 nm). Peak maxima  
346 are undergoing a slight shift due to solvatochromic effect, confirming that the fluorophore **3** is sensitive  
347 to its environment. The absorption spectrum of **NP3** (Fig. 1-D) shows a band in the 450-600 nm range,  
348 above the continuous scattering background created by the particles. To determine the exact position  
349 of band maximum and be able to compare **NP3** with **3**, the absorption spectrum of **NP2** was subtracted  
350 from **NP3** spectrum (Fig. 1-D). The resulting curve (green line) reveals the absorption profile observed  
351 for **3** in the **NP3** environment, with a peak maximum value at 520 nm slightly red-shifted. This  
352 demonstrates that after grafting on the particles, **3** is in a highly polar medium. Indeed, the subtracted  
353 spectrum (green line) and the absorption of **3** dissolved in EG are similar (Fig. 1-E) in good agreement  
354 with the fact that on the surface of the particle, **3** is surrounded by the PEG chains.

355 **Table 1** Relevant Spectroscopic properties of compound **3** in different solvents and **NP3** in water

	$\lambda_{\max}$ (nm)	$\varepsilon(\lambda_{\max})$ (mM <sup>-1</sup> cm <sup>-1</sup> )	$\lambda_{\text{em}}$ (nm) <sup>a</sup>	$\Delta\bar{\nu}$ (cm <sup>-1</sup> ) <sup>a</sup>	RQY <sup>a</sup>
<b>3</b>					
in DCM <sup>b</sup>	505	32800	634	4029	0.01
in ACN <sup>b</sup>	500	29200	653	4686	0.03
in MeOH <sup>b</sup>	507	37000	658	4527	0.12
<b>NP3</b>					
in H <sub>2</sub> O	520	–	682	4568	0.03
scattering corrected <sup>c</sup>					0.13

356 <sup>a</sup>  $\lambda_{\text{ex}} = 510$  nm, RQY: relative quantum yield; reference Erythrosine B <sup>30</sup> in methanol (QY<sub>Ref</sub> = 0.09)

357 <sup>b</sup> DCM: dichloromethane; ACN: acetonitrile; MeOH: methanol

358 <sup>c</sup> The absorption spectrum is corrected for scattering and the corrected absorbance value is used to determine the RQY.

359 Fluorescence emission and excitation spectra were recorded for fluorophore **3** in different solvents and  
360 in water for **NP3**. The spectroscopic results were summarized in Table 1. As it is shown in Fig. S6,  
361 fluorescence emission of **3** undergoes a positive solvatochromism (red-shifted maxima) upon increasing

362 solvent polarity; this is consistent with previous studies on similar dyes.<sup>25</sup> The maximum emission for  
363 **NP3** (Fig. 1-F) is also in agreement with the solvent polarity dependence of the free dyes' series (positive  
364 solvatochromism). Upon excitation at 510 nm of **NP3** in water, the maximum emission detected is  
365 centered at 682 nm. It is very unlikely that the highly lipophilic fluorophore **3** is surrounded by water  
366 molecules in the **NP3** configuration. Instead, the polar PEG chains on the particle surface offer a more  
367 favorable environment, which is in accordance with the previous observations from absorption  
368 spectroscopy (Fig. 1-E).

369 As mentioned before, absorbance of **NP3** is highly dominated by scattering. The absorbance value at  
370 the excitation wavelength ( $\lambda_{exc} = 510$  nm), used for relative quantum yield determination, results in an  
371 apparent quantum yield of only 3 %. However, by considering the subtracted spectrum, without  
372 scattering (Fig. 1-D, green line), a more realistic value of absorbance is obtained with a calculated  
373 quantum yield of 13 %. This value is in accordance with the results found for **3** in polar solvents such as  
374 methanol (Table 1), suggesting that the fluorescence of **3** is not altered upon the coupling to the  
375 particle.

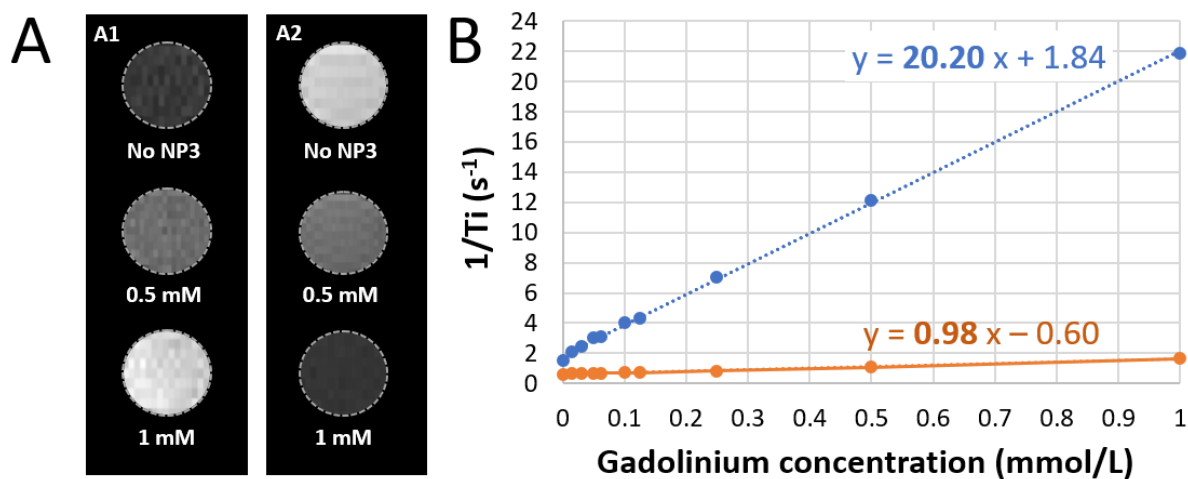
### 376 **Two-photon absorption (TPA) spectroscopic characterization of NP3**

377 Two-photon spectroscopic properties of **NP3** were evaluated prior to *in vivo* two-photon microscopy  
378 imaging. Characterization of the two-photon absorption (TPA) cross sections of **NP3** at different  
379 wavelengths was performed by measuring the two-photon induced excitation spectrum<sup>31,32</sup> and  
380 comparison to a known reference. The TPA spectrum of **NP3** was determined between 830 and  
381 1000 nm, the tuning range of the excitation source being limited to the maximum of 1000 nm.  
382 Consequently, only the blue-side of the TPA spectrum is characterized. According to the absorption  
383 spectrum corrected for scattering, the concentration of fluorophore **3** in **NP3** suspension used to  
384 evaluate the TPA cross-section values ( $\sigma_{TPA}$ ) is 16  $\mu$ M. At 980 nm, the excitation wavelength of our two-  
385 photon microscopy experiments, the  $\sigma_{TPA}$  is approximately 30 GM. This value is significantly lower than  
386 fluorophores of similar structures in solution.<sup>26</sup> This discrepancy is explained by the important decrease  
387 of the excitation and emission intensity due to the high scattering induced by particles in our TPA  
388 characterization configuration (see experimental details). For this reason, the normalized TPA spectrum  
389 of **NP3** is presented in Fig. 1-E (red scatter+line) and not the absolute  $\sigma_{TPA}$  values. As previously  
390 observed for the chromophore **3**,<sup>25</sup> this spectrum overlaps with the blue part of the linear absorption  
391 of **NP3**.

392 The TPA-induced fluorescence spectrum of **NP3**, shown in Fig. 1-F (yellow line), matches well with its  
 393 one-photon excited counterpart (Fig. 1-F, red line), showing that the fluorescence originates from the  
 394 same excited state in both cases. This observation justifies the use of the fluorescence detection for the  
 395 characterization of the TPA cross-section.

### 396 Magnetic resonance relaxivity measurements

397  $T_1$  and  $T_2$  relaxation time values were determined at 7 T in saline and at room temperature from  $T_1$  and  
 398  $T_2$  maps (Fig. 2-A). The  $r_1$  and  $r_2$  relaxivities of **NP3** were calculated, using the following formulas:  $1/T_1 = r_1 * C + 1/T_{1,0}$ ;  $1/T_2 = r_2 * C + 1/T_{2,0}$  ( $T_1$  and  $T_2$  in seconds;  $C$  = molar concentration in  $\text{mmol L}^{-1}$  and  $T_{1,0}$   
 399 and  $T_{2,0}$  are the relaxation times without contrast agent). A linear regression was made between the  
 400 gadolinium concentration (mM) of **NP3** phantoms and the associated values  $1/T_1$  or  $1/T_2$ . The slope of  
 401 the line represents  $r_1$  or  $r_2$  ( $\text{mM}^{-1} \text{s}^{-1}$ ), respectively (Fig. 2-B).



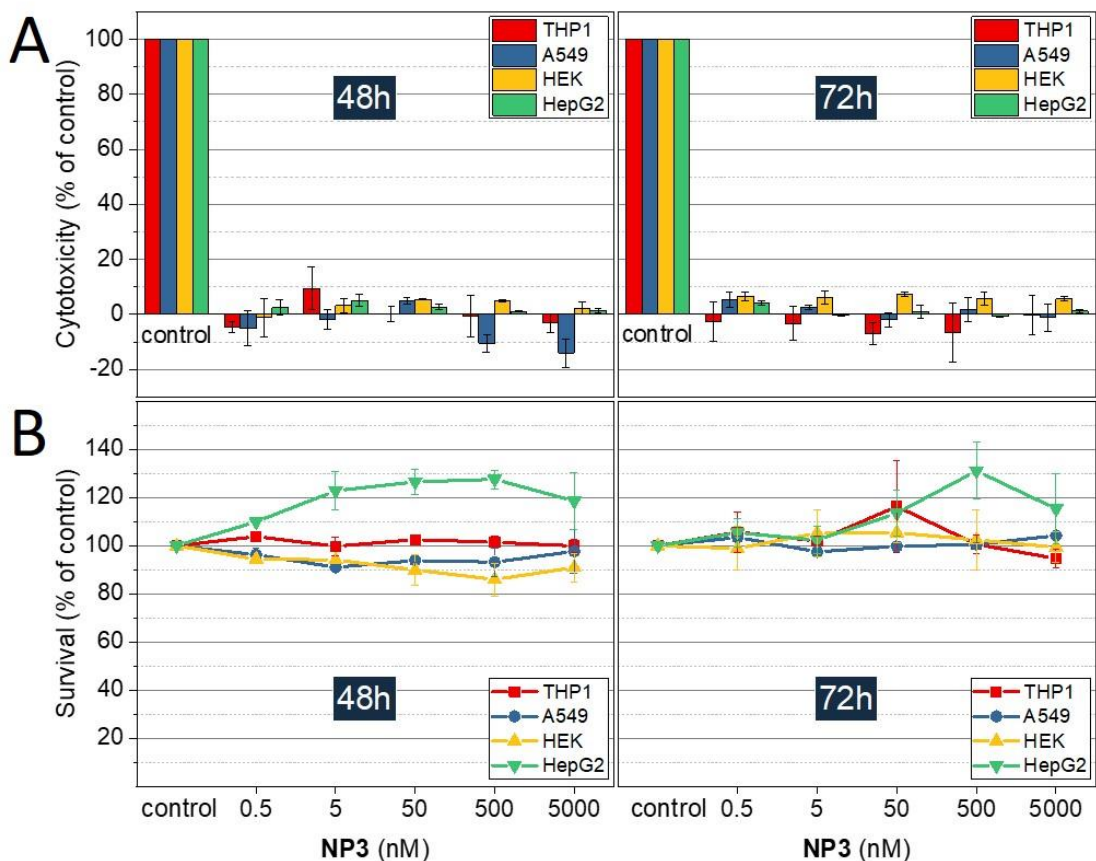
403 **Fig. 2 A) NP3** relaxivities. On  $T_1$ -weighted images, MR signal increases with gadolinium concentration increase (A1) whereas  
 404 on  $T_2$ -weighted images, MR signal drops with the increase of gadolinium concentration (A2). **B)** Measurement of  $r_1$  (orange)  
 405 and  $r_2$  (blue) relaxivities by linear regression connecting **NP3** phantoms gadolinium concentration to the value " $1/T_i$ ", where  
 406  $T_i$  means either  $T_1$  or  $T_2$ .  
 407

408 The estimated  $r_1$  and  $r_2$  relaxivities of **NP3** are  $0.98 \text{ mM}^{-1} \text{ s}^{-1}$  and  $20 \text{ mM}^{-1} \text{ s}^{-1}$ , respectively, leading to a  
 409  $r_2/r_1$  of 20.2. The  $r_2/r_1$  value found here is close to the value observed for the ultrasmall  
 410 superparamagnetic particles of iron oxide (USPIO), a well-known  $T_2/T_2^*$  MR contrast agent. Indeed, at  
 411 the same magnetic field, the  $r_2/r_1$  of the commercially available USPIO Ferumoxytol is 21.9.<sup>33</sup> Thus, **NP3**  
 412 appears to possess promising  $T_2/T_2^*$  contrast properties at the concentrations that are expected *in vivo*

413 and was further evaluated *in vivo* using  $T_2$  and  $T_2^*$ -weighted MR sequences, in line with our previous  
414 observations<sup>15</sup>

#### 415 ***In vitro* cytotoxicity assessment**

416 Toxicity is a major concern regarding nanoparticles used in bioimaging and especially when *in vivo*  
417 experiments are performed. In our specific case, prior to run *in vivo* imaging studies, the nanoparticle  
418 **NP3** cytotoxicity was evaluated on several human cell lines: THP-1 monocytes, HepG2 hepatocytes,  
419 A549 epithelial-like cells and HEK 293T kidneys cells. Two complementary assays, LDH and MTT, were  
420 used to investigate the potential impact of **NP3** on both mortality and metabolic activity of the cells  
421 incubated during 48h and 72h. The concentration of Gd in the culture medium ranges between 0 and  
422 5  $\mu\text{M}$ . All the LDH tests were compared to a positive control inducing 100% cell death. In all cases, the  
423 percentage of specific cytotoxicity is below 10% regardless of the cell lines, the **NP3** concentration or  
424 the incubation time (Fig. 3-A). In the case of the MTT assay, the metabolic activity of non-exposed cells  
425 was taken as reference of the survival and/or the proliferation of the cells (100%); all cell lines show a  
426 metabolic activity which remains constant, between 86 and 127%, independently of **NP3** concentration  
427 (Fig. 3-B).



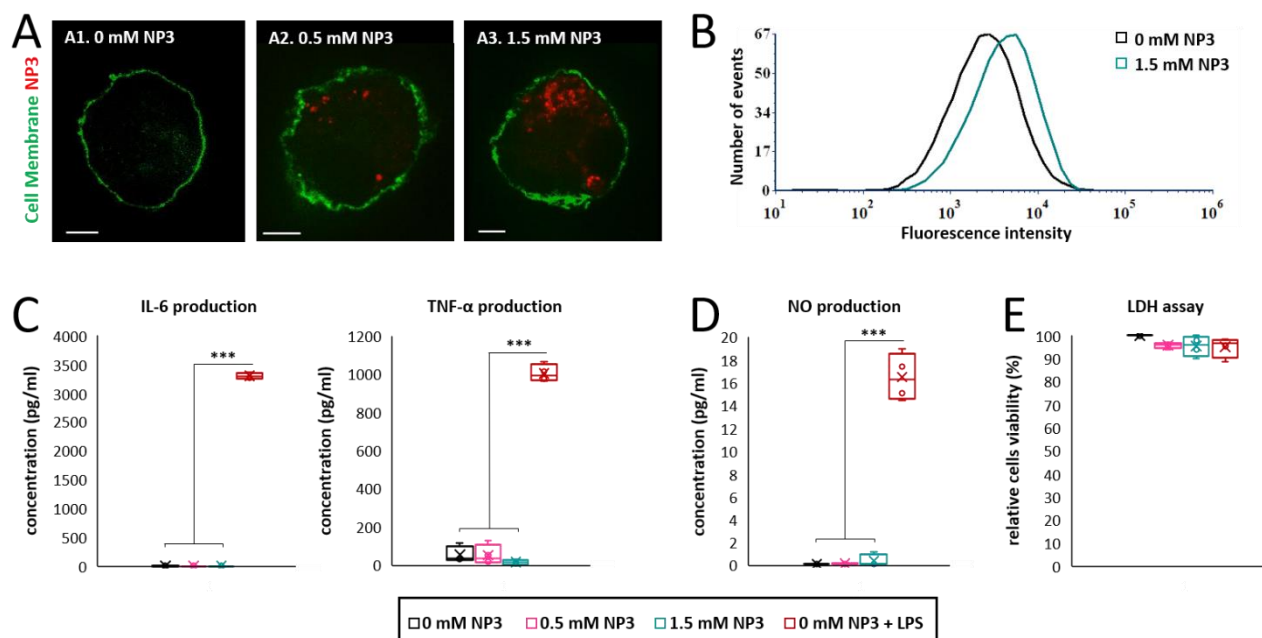
428

429 **Fig.3 Evaluation of NP3 cytotoxicity.** Cytotoxicity is measured in different human cultured cells: HepG2, HEK, A549 and  
 430 THP1. Cells are incubated with 0-5  $\mu\text{M}$  of NP3 for 48h and 72h. **A)** NP3 impact on cell survival assessed by LDH assay.  
 431 "Control" corresponds to the positive control with 100% cell death. Mean  $\pm$ SD of duplicates. **B)** NP3 effect on cell viability  
 432 assessed by MTT assay. Mean  $\pm$ SD of duplicates.

433 **NP3 is internalized by bone-marrow derived macrophages *in vitro* without overt toxic effects**

434 Internalization of NP3 particles by immune phagocytic cells was investigated *in vitro*. Bone marrow-  
 435 derived macrophage (BMDM) primary cultures were incubated with NP3 particles for 24h (technical  
 436 details are described in the *Supporting Material*). We first investigated the presence of the particle red  
 437 fluorescent signal with confocal microscopy. The confocal images showed an important accumulation  
 438 of nanoparticles inside the cells for 0.5 mM and 1.5 mM NP3 conditions (Fig. 4-A2 and 4-A3), but not in  
 439 the control condition (Fig. 4-A1). NP3 internalization measured by flow cytometry supported these  
 440 observations (Fig. 4-B). Pro-inflammatory cytokines, such as interleukine-6 (IL-6) and tumor-necrosis  
 441 factor- $\alpha$  (TNF- $\alpha$ ) play a key role in neuroinflammation. Therefore, we assessed their production by  
 442 BMDM cultures exposed to NP3 particles and compared it to IL-6 and TNF- $\alpha$  production by non-  
 443 exposed control BMDMs (Fig. 4-C). No significant difference has been observed for IL-6 and TNF- $\alpha$

444 production by **NP3**-treated and non-exposed cells. By contrast, BMDM exposed to lipopolysaccharide  
 445 or LPS (Fig. 4-C, red signal), used as a positive control for pro-inflammatory cytokine production, was  
 446 associated with significantly higher concentrations of IL-6 and TNF- $\alpha$ . This observation suggests that  
 447 **NP3** particles did not induce inflammation. In addition, BMDM exposure to **NP3** was not associated  
 448 with increase of nitric oxide (NO) concentration (Fig 4D), thus suggesting that **NP3** did not induce  
 449 oxidative stress either. Finally, cell viability was not affected by **NP3** exposure (Fig 4E).  
 450



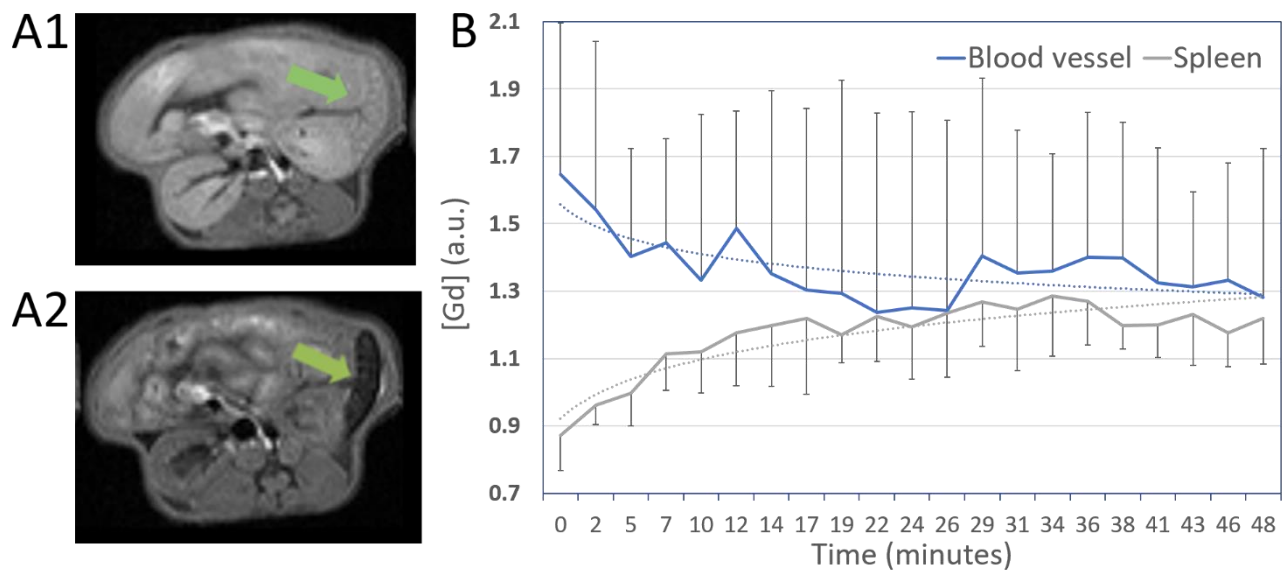
451

452 **Fig. 4 NP3 is internalized by BMDM and is not associated with cytotoxicity.** **A)** Confocal images of primary BMDM incubated  
 453 with **NP3** (A2, 0.5 mmol/L; A3, 1.5 mmol/L) or without **NP3** (A1). BMDM cell membranes labelled with FITC conjugated  
 454 cholera toxin are detected in green and **NP3** in red. (Scale bars: 5  $\mu$ m). **B)** Flow cytometer analysis shows the proportion of  
 455 BMDM cells positives for **NP3** for BMDM incubated with 1.5 mmol/L **NP3**. BMDM cells not incubated with **NP3** (0 mM **NP3**)  
 456 were used as control of **NP3** negative cells. **C)** Quantification of interleukin-6 (IL-6) and tumor-necrosis factor alpha (TNF- $\alpha$ )  
 457 production by BMDM exposed to **NP3**. **D)** Quantification of nitric oxide production by macrophages exposed to **NP3**. **E)**  
 458 Assessment of cell viability after exposition to **NP3**. For **C** to **E** experiments, cells exposed to LPS but not to **NP3** (condition  
 459 "0 mM **NP3** + LPS") were used as a positive control of inflammatory environment. Significant differences calculated with a  
 460 one-way ANOVA for n=4 independent experiments are indicated by \*\*\* for p < 0.005. w/o: without.  
 461

462 Altogether, these results (Fig. 3 and Fig. 4) demonstrate the lack of toxic effects of **NP3** on the fate of  
 463 the cells, highlighting the high level of safety of these nanoprobe and confirming their potential to be  
 464 used further for *in vivo* imaging of phagocytic cells.

465 **Biodistribution and pharmacokinetic profile of NP3**

466 Biodistribution and pharmacokinetic of **NP3** particles were evaluated *in vivo* in healthy mice by imaging  
 467 the abdominal area with dynamic MRI. There was only a slight enhancement in the kidneys. In contrast,  
 468 there was a strong accumulation of **NP3** in the spleen during the first hours after injection (Fig. 5-A),  
 469 and, to a lesser extent in the liver, such suggesting that **NP3** is taken up by phagocytic cells from the  
 470 reticuloendothelial system. From the vessel data (Fig. 5-B), we concluded that **NP3** has a long vascular  
 471 remanence (> 6h). Therefore, the post-**NP3** MRI scan was scheduled 48h post-injection to allow  
 472 sufficient time for nanoparticles elimination from the vascular compartment at the time of scanning.  
 473 The long vascular remanence is an advantage for accumulation of the contrast agent in the brain in  
 474 presence of a dysfunctional brain blood barrier as encountered in ischemic stroke. On the other hand,  
 475 further studies are warranted to further characterize the safety profile of NP3 and in particular its long-  
 476 term stability in serum and long-term fate after administration [3].  
 477



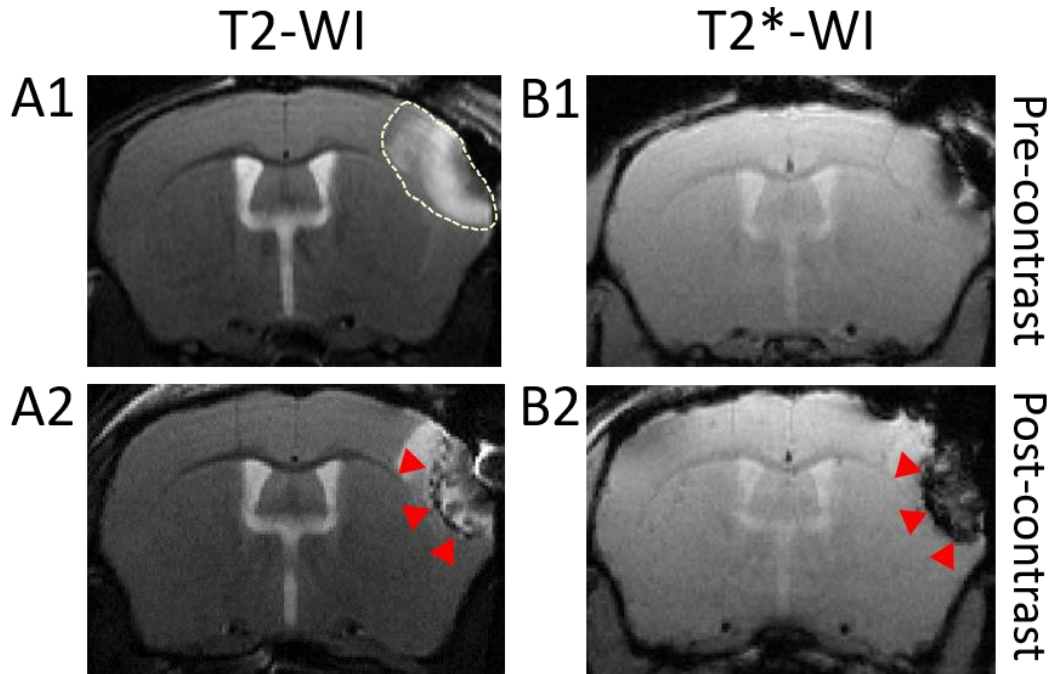
478

479 **Fig 5** Biodistribution and Pharmacokinetic. **A)** **NP3** biodistribution and pharmacokinetic were assessed with a dynamic  
 480 sequence in the abdomen. A1: before gadolinium injection and A2: after gadolinium injection, at the end of the dynamic  
 481 sequence. Green arrow points to the spleen. **B)** Graph represents the evolution of MR signal intensities due to gadolinium  
 482 associated with **NP3** in the spleen and the blood compartment across time after the first pass. Mean  $\pm$  SD (n = 4).

### 483 Multimodal imaging in a mouse model of ischemic stroke

484 Nanoparticle **NP3** was applied as a contrast agent for *in vivo* brain imaging in CX3CR1-GFP/+ mice with  
 485 green-fluorescent microglia/macrophages subjected to permanent middle cerebral artery (pMCAo).  
 486 The suspension of **NP3** was intravenously injected into the mouse tail vein at the dose of 2 mmol Gd/kg

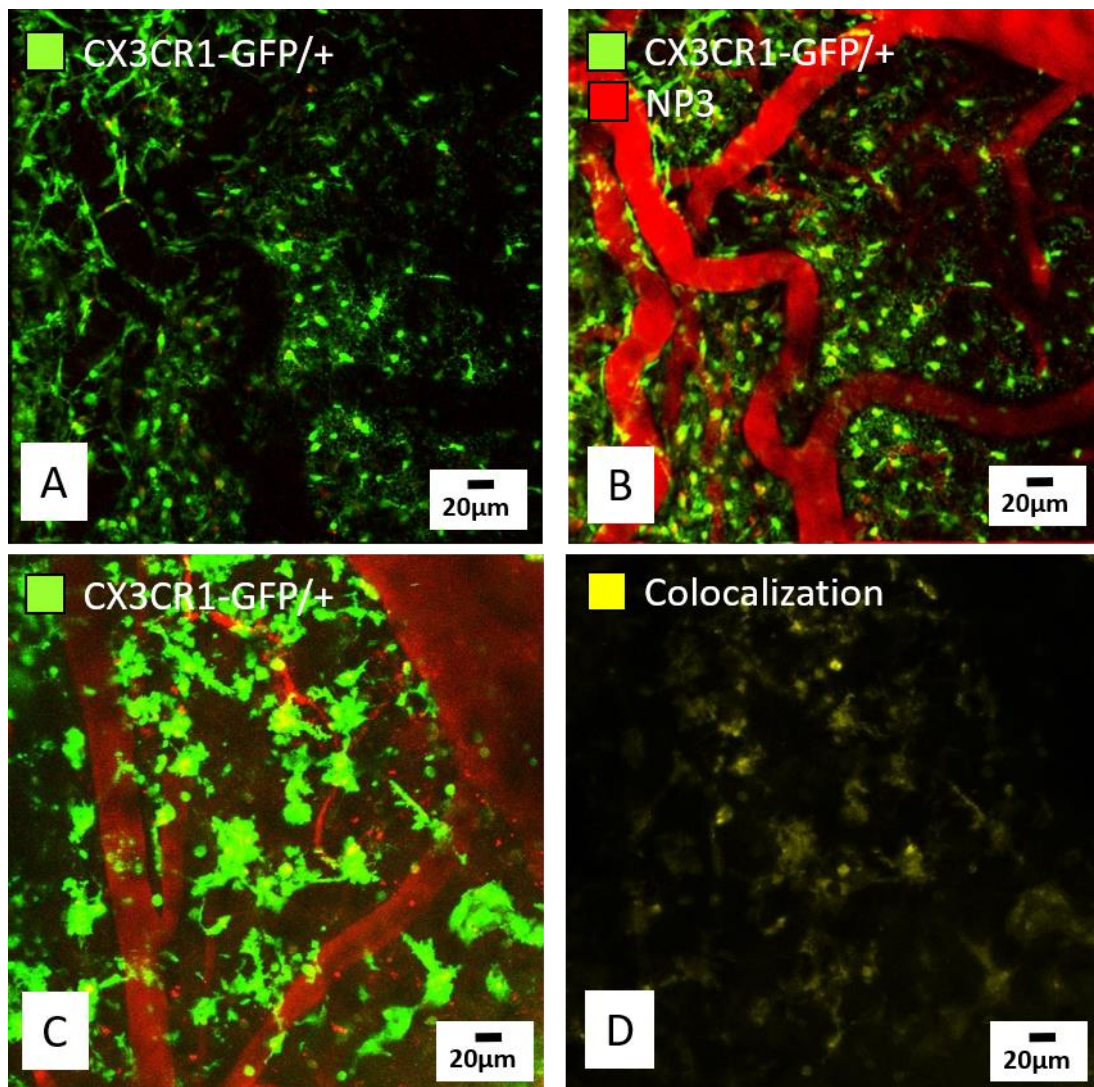
487 and the animal's brain was imaged with MRI and intravital two-photon excitation microscopy (TPEM),  
488 before and after the injection of the contrast agent.



489  
490 **Fig. 6** *In vivo* NP3-enhanced MRI. **A1, B1**) Pre- and **A2, B2**) post-NP3 injection T<sub>2</sub>- and T<sub>2</sub>\*-weighted images (WI) of a pMCAo  
491 mouse brain. The ischemic lesion is seen as a hyperintense signal in T<sub>2</sub>-WI (dotted line, A1). Accumulation of the  
492 nanoparticles in the ischemic area is characterized by the presence of hypointense signal voids in the lesion on post-NP3 T<sub>2</sub>-  
493 WI (A2, red arrowheads) and T<sub>2</sub>\*-WI (B2, red arrowheads).

494 Fig. 6 shows T<sub>2</sub>-weighted MR images (T<sub>2</sub>-WI) pre- and post-NP3 injection. The ischemic lesion appeared  
495 as a hyperintense signal (dotted line) in pre-NP3 T<sub>2</sub>-WI (Fig. 6-A1). On the T<sub>2</sub>-WI post-contrast images  
496 (Fig. 6-A2), signal voids due to the nanoprobe are clearly distinguished inside the lesional area (red  
497 arrowheads, ischemic core). Signal voids were also detected within the ischemic core on T<sub>2</sub>\*-WI (red  
498 arrowheads, Fig. 6-B2). This confirms the potential of NP3 as a T<sub>2</sub> and T<sub>2</sub>\* contrast agent and shows the  
499 ability of the probe to accumulate inside the ischemic lesion. The main advantages of this approach  
500 compared to nuclear imaging ones is three-fold: first, it allows the imaging at the acute stage of ischemic  
501 stroke (3 days post-onset) which is currently not achievable with PET coupled to the administration of  
502 TSPO tracers; second, it provides a better spatial resolution in the mouse brain together with accurate  
503 morphological lesion depiction; and third, it opens the way to longitudinal tracking of labelled  
504 macrophages without the need for additional injection.

505 TPEM imaging offers the possibility to observe the cortical area at the subcellular scale, completing  
506 whole-brain MR imaging.

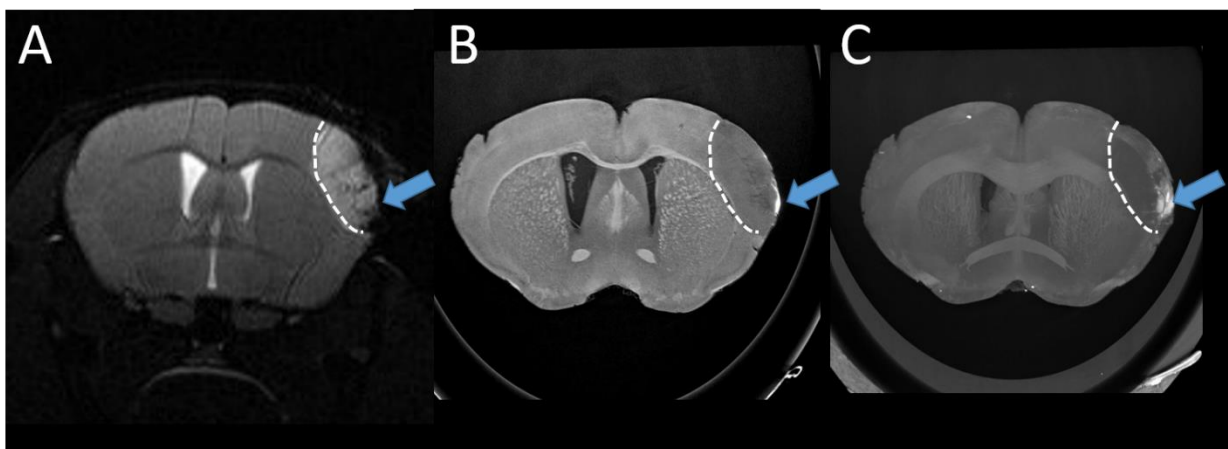


507

508 **Fig. 7** Observation of the **NP3** *in vivo* in different brain compartments using two-photon microscopy. **A, B)** Representative  
 509 images of the parenchyma and blood vessels pre- (A) and post-**NP3** injection (B) in a control mouse showing resting CX3CR1-  
 510 GFP/+ cells (in green) with ramified morphology. The nanoparticles (in red, B) are observed in the blood vessels immediately  
 511 after injection, but not in the brain parenchyma. **C)** In a pMCAo mouse, at the core of the lesion, the nanoparticles are  
 512 present in vessels and inside activated CX3CR1-GFP/+ cells. **D)** Nanoparticles are internalized by CX3CR1-GFP/+ cells: yellow  
 513 signal corresponds to the colocalization of CX3CR1-GFP/+ cells (green signal in C) and the nanoparticles (red signal in C).

514 In a first series of experiments, CX3CR1-GFP/+ cells were observed by intravital TPEM in the  
 515 parenchyma of a control mouse, as well as blood vessels that appear empty on the image before  
 516 injection of **NP3** (Fig. 7-A). Immediately after injection, an intense signal was detected in the blood  
 517 vessels, indicating the presence of nanoparticles in the blood flow (red signal in Fig. 7-B). Going further,  
 518 CX3CR1-GFP/+ mice subjected to pMCAo were imaged with TPEM. When looking at the core of the  
 519 ischemic lesion, **NP3** nanoparticles were observed in blood vessels (Fig. 7-C) and an important number  
 520 of CX3CR1-GFP/+ cells colocalized with the **NP3** fluorescent signal (yellow signal in Fig. 7-D), suggesting

521 that the nanoparticles are effectively internalized by activated microglial cells and macrophages. Thus,  
522 the **NP3**-labeled cells become visible and directly observable in TPEM. Of note, the nanoparticles were  
523 still detected with TPEM in the blood vessels 24h post-**NP3** administration (Fig. S7), further confirming  
524 the long (> 6 h) vascular remanence of **NP3** observed during the pharmacokinetic study.



525

526 **Fig. 8** *In vivo*  $T_2$ -WI image **A**) and ex vivo phase-contrast computed tomography images **B-C**) for the same pMCAo mouse  
527 injected with **NP3**. Hypointense signals on *in vivo*  $T_2$ -WI (A, blue arrow) colocalizes with hyperdense signals observed on  
528 native image (B, blue arrow) and maximum intensity projection (MIP) obtained with phase contrast image (C, blue arrow)  
529 and corresponding to the presence of Gd in the lesion. Dotted white line delineate the ischemic lesion.

530 In order to ascertain that **NP3** nanoparticle was stable *in vivo* and hence that the  $GdF_3$  core was also  
531 found in the brain parenchyma (i.e. in the regions where we detected the red fluorescence of the  
532 grafted fluorophore), mice brains have been perfused to wash out the vascular sector, sampled and  
533 scanned with synchrotron radiation phase contrast imaging. This innovative technique is based on the  
534 imaging of X-ray refraction rather than absorption thus resulting in enhanced contrast of soft tissues  
535 while allowing the accurate detection of metal-based contrast agents in the whole brain at microscale-  
536 resolution.<sup>14,34</sup> The gadolinium of **NP3** nanoparticles are clearly seen inside the ischemic lesion as a  
537 hyperintense signal that co-localizes with MR signal voids (Fig. 8). In summary, **NP3**-labeled  
538 macrophages could be imaged with three complementary imaging modalities, at different scales: MRI  
539 ( $\sim 100\text{-}\mu\text{m}$ ), intravital microscopy ( $\sim 10\text{-}\mu\text{m}$ ) and synchrotron x-rays ( $\sim 1\text{-}\mu\text{m}$ ). Such multi-scale approach  
540 is crucial in order to decipher the macrophage response at the early stage of ischemic stroke.

## 541 **Conclusions**

542 A hybrid  $GdF_3$  contrast agent **NP3** was developed and fully characterized for multimodal and multiscale  
543 imaging of phagocytic cells. The inorganic core composed of highly crystalline  $GdF_3$ , one of the most

544 stable compounds of gadolinium, shows good properties for MR and X-ray imaging. The PEG layer  
545 strongly anchored to the particle through bisphosphonate moieties confers biostability to the  
546 nanoparticle. **NP3** has a relatively small hydrodynamic diameter, a long vascular remanence and a  
547 negative zeta potential, all properties which are known to be associated with greater uptake by  
548 macrophages.<sup>35,36</sup> *In vitro* cytotoxicity assessments performed on four human cell lines and on bone  
549 marrow-derived macrophages revealed no toxic effects. A two-photon active red-fluorophore coupled  
550 to the PEG-functionalized nanoparticle provided additive efficient contrast-enhancement properties for  
551 *in vivo* two-photon fluorescence imaging with resolution at the molecular scale.

552 The proof-of-concept that **NP3** nanoparticle may be used as a contrast agent targeting phagocytic cells  
553 was provided *in vitro* using bone-marrow derived macrophages and *in vivo* in an animal model of  
554 ischemic stroke using transgenic CX3CR1-GFP/+ mice. *In vivo* mouse brain MR imaging revealed the  
555 accumulation of the particles in the ischemic lesion, which is further confirmed by post-mortem *ex vivo*  
556 synchrotron radiation phase contrast imaging. The presence of the particles inside phagocytic cells was  
557 evidenced *in vivo* by TEM observations, which indicates the internalization of the contrast agent by  
558 cells involved in neuroinflammation. Full validation of the imaging approach in a preclinical study of  
559 mice with ischemic stroke is ongoing.<sup>37</sup> The next step will be to take advantage of gadolinium for specific  
560 imaging with spectral photon counting CT in order to eliminate the need for pre-contrast scanning. Both  
561 these imaging approaches are technically challenging due to their lower sensitivity, therefore  
562 necessitating further dedicated developments. Nevertheless, our results clearly demonstrate the  
563 preclinical potential of hybrid GdF<sub>3</sub> nanoparticles as a promising tool for imaging phagocytic cells in  
564 neuroinflammatory diseases with multiscale resolution from macroscopic down to cellular level. Such  
565 preclinical imaging tool is crucial to select the immunomodulatory treatments that reach their target  
566 and may thus be translated into the clinics.

567 **Authors contributions:** SP and MW designed and supervised the project. SK, FL, FC and SP designed,  
568 synthesized and characterized the nanoparticle. YB and CA designed the fluorophore. SK, Y.B, GM, AB  
569 and MLI performed the optical characterizations. MM and MLe designed the PEG ligands. AD, MMR and  
570 PNM assessed nanotoxicity. IH and OP realized the *in vivo* two-photon imaging and interpreted the  
571 data. VH and MW performed the MR imaging experiments and interpreted the data. VH and IH

572 performed the surgeries. SK, VH, IH, FL, SP, MW and OP wrote the article. All authors approved the final  
573 version of the manuscript.

#### 574 **Conflicts of interest**

575 There are no conflicts of interest to declare.

#### 576 **Acknowledgements**

577 This study was supported by the Agence Nationale de la Recherche (ANR) (Project Nanobrain, grant #  
578 ANR-15-CE18-0026-01). The authors acknowledge the contribution of SFR Biosciences  
579 (UMS3444/CNRS, US8/Inserm, ENS de Lyon, UCBL) facilities PLATIM, especially Claire Lionnet, for  
580 assistance with the femtosecond laser system. Clémence Gaudin is acknowledged for help with the  
581 cytotoxicity evaluations. We thank Lyon's multimodal imaging platform Cermep and the engineers that  
582 have helped us perform MR imaging: Jean-Baptiste Langlois and Radu Bolbos. We acknowledge the  
583 European Synchrotron Radiation Facility for allocation of beamtime (MD1094) and we would like to  
584 thank Emmanuel Brun and Hélène Elleaume for performing acquisitions on Medical Beamline ID17 and  
585 phase contrast image reconstruction. The authors acknowledge *Science et Surface* for help with XPS  
586 characterization.

587

588

589 **References**

- 590 1 Feigin Valery L., Norrving Bo, and Mensah George A., *Circ. Res.*, 2017, **120**, 439–448.
- 591 2 U. Dirnagl, C. Iadecola and M. A. Moskowitz, *Trends Neurosci.*, 1999, **22**, 391–397.
- 592 3 Q. Wang, X. N. Tang and M. A. Yenari, *J. Neuroimmunol.*, 2007, **184**, 53–68.
- 593 4 A. Ciarmiello, *Eur. J. Nucl. Med. Mol. Imaging*, 2011, **38**, 2198–2201.
- 594 5 C. Corot, K. G. Petry, R. Trivedi, A. Saleh, C. Jonkmanns, J.-F. Le Bas, E. Blezer, M.
- 595 Rausch, B. Brochet, P. Foster-Gareau, D. Balériaux, S. Gaillard and V. Dousset, *Invest.*
- 596 *Radiol.*, 2004, **39**, 619–625.
- 597 6 P. Chhour, P. C. Naha, S. M. O’Neill, H. I. Litt, M. P. Reilly, V. A. Ferrari and D. P.
- 598 Cormode, *Biomaterials*, 2016, **87**, 93–103.
- 599 7 M. N. Bouchlaka, K. D. Ludwig, J. W. Gordon, M. P. Kutz, B. P. Bednarz, S. B. Fain and
- 600 C. M. Capitini, *Oncoimmunology*, 2016, **5**, e1143996.
- 601 8 S. Si-Mohamed, D. Bar-Ness, M. Sigovan, V. Tatard-Leitman, D. P. Cormode, P. C.
- 602 Naha, P. Coulon, L. Rasclé, E. Roessl, M. Rokni, A. Altman, Y. Yagil, L. Bousset and P.
- 603 Douek, *Eur. Radiol. Exp.*, 2018, **2**, 34.
- 604 9 M. L. Cotrina, N. Lou, J. Tome-Garcia, J. Goldman and M. Nedergaard, *Neuroscience*,
- 605 2017, **343**, 483–494.
- 606 10 M. P. Menon and J. James, *J. Chem. Soc. Faraday Trans. 1 Phys. Chem. Condens.*
- 607 *Phases*, 1989, **85**, 2683.
- 608 11 N. Halttunen, F. Lerouge, F. Chaput, M. Vandamme, S. Karpati, S. Si-Mohamed,
- 609 M. Sigovan, L. Bousset, E. Chereul, P. Douek and S. Parola, *Sci. Rep.*, 2019, **9**, 12090.
- 610 12 S. de Reguardati, J. Pahapill, A. Mikhailov, Y. Stepanenko and A. Rebane, *Opt.*
- 611 *Express*, 2016, **24**, 9053–9066.
- 612 13 H. Karatas, S. E. Erdener, Y. Gursoy-Ozdemir, G. Gurer, F. Soylemezoglu, A. K.
- 613 Dunn and T. Dalkara, *J. Cereb. Blood Flow Metab.*, 2011, **31**, 1452–1460.
- 614 14 M. Marinescu, M. Langer, A. Durand, C. Olivier, A. Chabrol, H. Rositi, F.
- 615 Chauveau, T. H. Cho, N. Nighoghossian, Y. Berthezène, F. Peyrin and M. Wiart, *Mol.*
- 616 *Imaging Biol.*, 2013, **15**, 552–559.
- 617 15 F. Mpambani, A. K. O. Åslund, F. Lerouge, S. Nyström, N. Reitan, E. M. Huuse, M.
- 618 Widerøe, F. Chaput, C. Monnerieu, C. Andraud, M. Lecouvey, S. Handrick, S. Prokop,
- 619 F. L. Heppner, P. Nilsson, P. Hammarström, M. Lindgren and S. Parola, *ACS Appl. Bio*
- 620 *Mater.*, 2018, **1**, 462–472.
- 621 16 F. Chaput, F. Lerouge, S. Tusseau-Nenez, P.-E. Coulon, C. Dujardin, S. Denis-
- 622 Quanquin, F. Mpambani and S. Parola, *Langmuir*, 2011, **27**, 5555–5561.
- 623 17 EP2445838 (A1), 2009.
- 624 18 E. Ringe, R. P. Van Duyne and L. D. Marks, *Nano Lett.*, 2011, **11**, 3399–3403.

- 625 19 S. Kachbi-Khelfallah, M. Monteil, M. Cortes-Clerget, E. Migianu-Griffoni, J.-L.  
626 Pirat, O. Gager, J. Deschamp and M. Lecouvey, *Beilstein J. Org. Chem.*, 2016, **12**,  
627 1366–1371.
- 628 20 Z.-Y. Yang, S.-L. Luo, H. Li, S.-W. Dong, J. He, H. Jiang, R. Li and X.-C. Yang, *RSC*  
629 *Adv*, 2014, **4**, 59965–59969.
- 630 21 L. Sandiford, A. Phinikaridou, A. Protti, L. K. Meszaros, X. Cui, Y. Yan, G.  
631 Frodsham, P. A. Williamson, N. Gaddum, R. M. Botnar, P. J. Blower, M. A. Green and  
632 R. T. M. de Rosales, *ACS Nano*, 2013, **7**, 500–512.
- 633 22 S. Redon, J. Massin, S. Pouvreau, E. De Meulenaere, K. Clays, Y. Queneau, C.  
634 Andraud, A. Girard-Egrot, Y. Bretonnière and S. Chambert, *Bioconjug. Chem.*, 2014,  
635 **25**, 773–787.
- 636 23 Z. Varga, J. Mihály, Sz. Berényi and A. Bóta, *Eur. Polym. J.*, 2013, **49**, 2415–2421.
- 637 24 R. Lemke, *Synthesis*, 1974, **1974**, 359–361.
- 638 25 J. Massin, W. Dayoub, J.-C. Mulatier, C. Aronica, Y. Bretonnière and C. Andraud,  
639 *Chem. Mater.*, 2011, **23**, 862–873.
- 640 26 J. Massin, A. Charaf-Eddin, F. Appaix, Y. Bretonnière, D. Jacquemin, B. van der  
641 Sanden, C. Monnereau and C. Andraud, *Chem. Sci.*, 2013, **4**, 2833.
- 642 27 R. Huisgen, *Angew. Chem. Int. Ed. Engl.*, 1963, **2**, 565–598.
- 643 28 H. J. Benyettou F, *J. Bioanal. Biomed.*, 2012, **04**, 39.
- 644 29 J. F. Moulder and J. Chastain, Eds., *Handbook of X-ray photoelectron*  
645 *spectroscopy: a reference book of standard spectra for identification and*  
646 *interpretation of XPS data*, Perkin-Elmer Corporation, Eden Prairie, Minn, Update.,  
647 1992.
- 648 30 N. Boens, W. Qin, N. Basarić, J. Hofkens, M. Ameloot, J. Pouget, J.-P. Lefèvre, B.  
649 Valeur, E. Gratton, M. vandeVen, N. D. Silva, Y. Engelborghs, K. Willaert, A. Sillen, G.  
650 Rumbles, D. Phillips, A. J. W. G. Visser, A. van Hoek, J. R. Lakowicz, H. Malak, I.  
651 Gryczynski, A. G. Szabo, D. T. Krajcarski, N. Tamai and A. Miura, *Anal. Chem.*, 2007,  
652 **79**, 2137–2149.
- 653 31 C. Xu and W. W. Webb, *JOSA B*, 1996, **13**, 481–491.
- 654 32 N. S. Makarov, J. Campo, J. M. Hales and J. W. Perry, *Opt. Mater. Express*, 2011,  
655 **1**, 551–563.
- 656 33 S. Liu, J.-C. Brisset, J. Hu, E. M. Haacke and Y. Ge, *J. Magn. Reson. Imaging*, 2018,  
657 **47**, 621–633.
- 658 34 J. Albers, S. Pacilé, M. A. Markus, M. Wiart, G. Vande Velde, G. Tromba and C.  
659 Dullin, *Mol. Imaging Biol.*, 2018, **20**, 732–741.
- 660 35 C. Corot, P. Robert, J.-M. Idée and M. Port, *Adv. Drug Deliv. Rev.*, 2006, **58**, 1471–  
661 1504.
- 662 36 E. Fröhlich, *Int. J. Nanomedicine*, 2012, **7**, 5577–5591.

663 37 V. Hubert, I. Hristovska, S. Karpati, S. Benkeder, C. Dumot, C. Amaz, N.  
664 Chounlamountri, C. Watrin, J.-C. Comte, F. Chauveau, E. Brun, F. Lerouge, S. Parola,  
665 O. Pascual and M. Wiart, .Paper on preparation

- 666  
667  
668 1. Zinnhardt, B., et al., Theranostics, 2018. **8**(10): p. 2603-2620.  
669 2. Schirra, C.O., et al., Contrast Media Mol Imaging, 2014. **9**(1): p. 62-70.  
670 3. Tamion, A., et al., Nano Research, 2016. **9**(8): p. 2398-2410.

671  
672